Triple junction solute segregation in Al-based polycrystals

Nutth Tuchinda and Christopher A. Schuh

Phys. Rev. Materials **7**, 023601 — Published 16 February 2023

DOI: 10.1103/PhysRevMaterials.7.023601

Triple Junction Solute Segregation in Al-based Polycrystals

Nutth Tuchinda[1], Christopher A. Schuh[1*]

[1]Department of Materials Science and Engineering, Massachusetts Institute of Technology, 77 Massachusetts Avenue, Cambridge, MA, 02139, USA

***Correspondence to: schuh@mit.edu**

Abstract

Solute segregation is a crucial means of stabilizing nanostructured alloys, and at very small grain sizes this requires consideration of triple junctions, which attain a meaningful volume fraction and thus become relevant for bulk material behavior. Here the solute segregation spectra for grain boundary and triple junction sites are calculated for a large number of dilute Al-based binary systems with available interatomic potentials. A defect-identifying algorithm is applied to quantify the average grain boundary thickness and classify the intergranular site spectra into grain boundary and junction subspectra. The algorithm is also applied to a hybrid electronic-level database for grain boundary segregation of various solutes in Al, yielding polycrystalline triple junction solute segregation spectra from first principles for the first time. The results suggest that triple junction segregation is alloy- or interatomic potential-dependent and can exhibit either boundary or junction preference. With these spectra as inputs, the spectral grain boundary segregation model gives quantitative predictions of segregation as a function of grain size, temperature and total solute concentration, suitable for alloy screening and design.

Keywords: Grain Boundary, Triple junction, Quadruple Node, Segregation, Nanocrystalline, Thermodynamics, Atomistic Simulation

---

I. Introduction

Nanocrystalline alloys [1,2] have shown promising properties for, e.g., mechanical applications [3–7], but generally need to be stabilized against grain growth [8]. The stability of nanocrystalline alloys depends on both the thermodynamics and kinetics of grain boundaries, each of which can be improved by decorating grain boundaries with solute atoms to lower the grain boundary network energy [9–13] and cause solute drag [14–18]. The understanding of solute segregation is therefore a fundamental input to achieving stabilized nanocrystalline alloys.

Intergranular segregation is often modeled in the dilute limit with the classical McLean isotherm [19]:

$$\frac{\bar{X}^{IG}}{1-\bar{X}^{IG}} = \frac{X^{C}}{1-X^{C}} exp\left[-\frac{\Delta\bar{E}_{eff}^{seg}}{k_{b}T}\right] \tag{1}$$

where $\bar{X}^{IG}$ and X^C are the average intergranular (IG) and crystalline (C) solute concentrations. $\Delta\bar{E}_{eff}^{seg}$ is the effective or average segregation energy of the system, which has often historically been assumed to be a single-value quantity. However, acknowledging the wide range of different sites in an IG network, White and Stein have shown that a similar isotherm which treats $\Delta\bar{E}_{eff}^{seg}$ as a distribution can be developed as [20]:

$$\frac{X_i^{IG}}{1-X_i^{IG}} = \frac{X^C}{1-X^C} exp\left[-\frac{\Delta E_i^{seg}}{k_b T}\right] \tag{2}$$

where X_i^{IG} describes the solute concentration at site type 'i' with local segregation energy ΔE_i^{seg}. The segregation energy is defined with respect to a crystalline site:

$$\Delta E_i^{seg} = E_i^{IG} - E^C \tag{3}$$

where E_i^{IG} and E^C are the energy of the system when a solute occupies an intergranular site 'i' and bulk crystalline site respectively, and a negative energy favors segregation.

While we can expect that ΔE_i^{seg} spans a large space of many distinct grain boundary sites [21–27], Wagih and Schuh have demonstrated that polycrystalline segregation energy spectra can be described remarkably well using a simple skew-normal distribution with three distribution parameters for the shape (α), location (μ), and scale (σ) of the distribution [28,29]:

$$F_i = \frac{1}{\sqrt{2\pi}\sigma} \exp\left[-\frac{\left(\Delta E_i^{seg} - \mu\right)^2}{2\sigma^2}\right] erfc\left[\frac{\alpha\left(\Delta E_i^{seg} - \mu\right)}{\sqrt{2}\sigma}\right] \tag{4}$$

Here F_i is the intergranular site probability density function. The shape of this spectrum for grain boundary segregation has been computed for many binary alloys with available interatomic potentials and tabulated in Ref. [30].

In the nanocrystalline limit, it is not only grain boundaries that contribute to segregation thermodynamics, but also the grain boundary junctions. The volume fraction of triple junctions becomes large below about 20 nm in grain size, which is a very important and interesting size range where, e.g., new mechanisms come into play and evoke engineering interest [31–35]. As a result of this, the total segregation energy distribution of Eq. (4) can become grain size dependent as the prominence of junctions increases [31,33,36–41]. In our previous work [42], we have explored this issue using molecular statics and found that the form of Eq. (4) can also be used to separately model the distributions of segregation for triple junctions and quadruple nodes; the various intergranular defect populations can then be considered separately and handled rigorously at any grain size.

In that prior work, we explored only a single system, Al(Mg), so apart from the validation that there are separable junction segregation subspectra, there remain many open questions about the generality of triple junction segregation in other systems. What is more, recent progress with Eq. (4) has extended the computation of segregation spectra to first-principles accuracy, which opens the door to a discussion about what features of interatomic potentials are physical or not for the phenomenon of intergranular segregation at grain junctions. In this paper, we extend the study of grain boundary junction solute segregation for 23 embedded atom method (EAM) [43–60] and 39 hybrid first-principles (quantum mechanical-molecular mechanical or QM-MM) Al(X) systems [61]. The result is a first significant database of segregation spectra for triple junction segregation for future alloy design and optimization. What is more, the results also introduce two physically different classes of alloy systems, i.e., those that have a natural preference for either grain boundary or triple junction segregation.

II. Methods

For the purpose of calculating the distribution of ΔE_i^{seg} as the input for the thermodynamic model in Eq. (2), pure Al polycrystals are generated using Atomsk [62] with 10 grains. We then scale and anneal the polycrystals following Ref. [42] using corresponding Al-based EAM potentials [63,64] for 23 Al(X) binary systems with 12 different solutes [44–60,65]. Typical atomic structures and the misorientations of all the grain boundaries (same in all samples) are shown in Fig. 1a along with the scaled Al(Sm) polycrystals in Fig. 1b-e. Molecular statics and dynamics calculations are conducted using the Large-scale Atomic/Molecular Massively Parallel Simulator (LAMMPS) software package [66–69], and the structural analysis is conducted in OVITO [70]. E_i^{IG} and E^C in Eq. (3) are calculated based on direct solute substitution in defect vs. crystalline sites following Ref. [42].

First-principles data on solute segregation in polycrystals are obtained by first applying our defect-identifying algorithm to the polycrystalline data from Ref. [61] calculated via the hybrid method, and then extracting GB and TJ subspectra for 39 Al(X) systems (i.e. we analyze the segregation distributions from Ref. [61]; no hybrid first-principles calculations are performed herein).

In order to classify a defect type, i.e. whether a given intergranular site is a grain boundary (GB) or triple junction (TJ) site, we first segment the polycrystals into multiple grains. This is done with the grain segmentation algorithm of Ref. [71] with polyhedral template matching [72]. Then we execute a nearest neighbor search around the site and construct a list of unique grain numbers; each atom is assigned a single grain number. Defect sites are identified by the grain numbers in their near proximity: a site with a single grain number amongst all of its nearest neighbors lies within a crystal; if there are two or three unique grain numbers, the site is identified as a GB or TJ site, respectively. We note that in our previous work we also considered the quadruple nodes as possible unique sites (with four grain numbers in the same neighborhood), but these are of negligible consequence except in the extreme limit at grain sizes of less than approximately 5 nm [73], and even then their segregation differences with respect to the TJ sites are not always significant [42]. Therefore, in this work the quadruple nodes are effectively rolled into the TJ network and treated as a part of it, without a significant loss of physics.

While we can directly apply the above algorithm to any polycrystalline structure, the arbitrary choice of neighbor grain search distance impacts the junction site population. We therefore adopt a calibration procedure: we first identify the intergranular sites by an adaptive common neighbor analysis [74,75], and then apply the segmentation algorithm using a range of cutoff radii. We define an intergranular network dimension (*t*), which in the limit of large grains is the average grain boundary thickness, as twice the value of the segmentation cutoff radius when the intergrain population converges to 99.5% of the large cutoff limit. This procedure is illustrated in Fig. 2 for the Al(Sm) system. The intergranular site fraction is shown as a function of cutoff radius in (a), with an illustration of the junction structure for a (b) overdetermined and (c) appropriately-determined case. The overdetermined case (b) shows TJ atoms protruding into the GB regions, meaning that atoms more properly belonging to the GBs are incorrectly attributed to the TJs; this can obviously cause errors in calculating the subspectra for both defect types, and especially risks blurring any difference between them. For every Al(X) system calculated, the site fraction saturates around ~0.5 nm as seen in Fig. 2(a), which is to say that the grain boundary thickness *t* has roughly the same magnitude for all interatomic potentials at approximately 1-1.2 nm. The results have been tabulated in Supplementary Table SI [76]. We use these values in what follows to cleanly separate junction solute segregation spectra in this study.

Our methods have been validated in a number of ways, by comparing with our own previous study on the Al-Mg system and exploring the role of different grain boundary and triple junction populations, and considering the role of simulated grain size on the outputs of the analysis, etc. These validations are explained in more detail in the Supplementary Material SM. 1 [76].

The only system previously investigated for TJ vis-à-vis GB segregation was Al(Mg) in Ref. [42]. One interesting and potentially important feature of the Al(Mg) system is that the triple junctions showed a stronger segregation tendency than the GBs that connect at them. This makes some intuitive sense for close packed metals in which the drive for segregation is often dominated by elastic mismatch and the need for excess free volume to accommodate solute. However, it is not clear whether this behavior observed in Al(Mg) can be considered canonical, and a scan of multiple Al(X) systems provides an opportunity to check. We therefore define a triple junction solute preference index J_X for the system *X* as follows:

$$J_X = \frac{Mean\left[\Delta E_{i,GB}^{seg}\right] - Mean\left[\Delta E_{i,TJ}^{seg}\right]}{\sqrt{Mean\left[{\Delta E_{i,GB}^{seg}}^2\right] - Mean\left[\Delta E_{i,GB}^{seg}\right]^2}} \tag{5}$$

where "Mean" is the average of the quantity from all GB or TJ sites, and is not the same as the distribution parameter μ from a skew-normal distribution of Eq. (4). (Means in Eq. (5) do not depend on the fitting method.) This expression captures the relative difference between the means of the TJ and GB subspectra (expressed as the expected value of $\Delta E_{i,TJ}^{seg}$ and $\Delta E_{i,GB}^{seg}$) in the numerator, normalized by the width of the GB subspectrum or the standard deviation in the denominator. The motivation of this index is to include the relative magnitude of the shift compared to the distribution shape since the equilibrium segregation content is a function of spectral shape parameter [28,42] (full thermodynamic quantitative analysis will be discussed in section 4). The value of J_X is positive when the solute prefers TJ sites to those of the GBs, and negative when the system favors GB segregation; in a single parameter it thus denotes which defect type would be expected to dominate the segregation behavior of the system. In principle, these values of J_x should correlate with experimental observations in systems where both grain boundary and triple junction concentrations are measured; such data are not common as yet, but it is hoped that future studies could provide experimental contact.

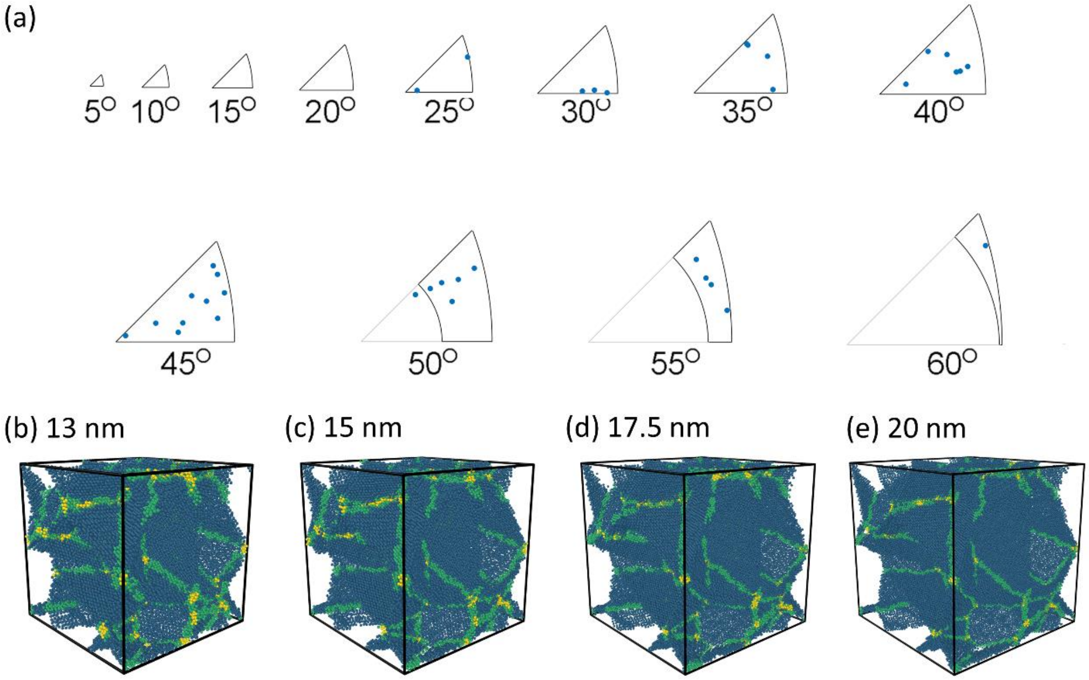

FIG. 1. (a) Misorientation plot for all 39 GBs in the polycrystalline samples explored here. (b-e) Self-similarly scaled Al(Sm) [59] polycrystals from 13-20 nm systems are visualized with the bulk atoms omitted. The atomic defect types are labeled via the color shade (dark green for grain boundaries, light green for triple junctions and yellow for quadruple nodes).

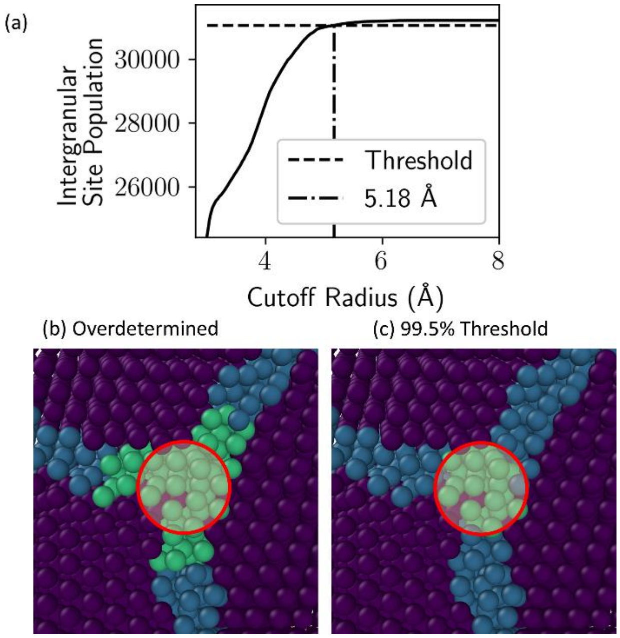

FIG. 2. (a) Intergranular site population identified by the algorithm with varying cutoff radius. The dashed vertical line indicates the cutoff where the population reaches 99.5% of the large cutoff limit. The structures shown in (b) and (c) are examples of the overdetermined and appropriately-determined cases respectively, with cutoff radii of 10 and 5.18 Å, respectively in the case of Al(Sm) [59].

III. Segregation Subspectra

A. Segregation Subspectra in EAM Al Alloy Systems

With these methods we proceed to analyze 23 EAM Al(X) systems for which there are published interatomic potentials from Refs. [44–60,65]. The computed segregation spectra are shown in Fig. 3. Here both the GB and TJ subspectra are explicitly shown, but the dominant distribution (i.e., the dominant coloration of the plot) is based on the value of the J_X index. We highlight in orange those TJ subspectra that outweigh the GB spectra (with a positive J_X index). The opposite scheme with blue coloration is used for the negative index systems in which the GBs outcompete the TJs for solute. While the majority of these systems have stronger TJ segregation than GB segregation, interestingly, a number of these systems show the opposite behavior: the Al(Co, Cr, Fe, Ni) systems [44] and Al(Ag) [43] all prefer GB segregation over TJ segregation. Since this behavior may be artificial due to the transferability of the potentials, we turn our attention to the QM-MM results from Ref. [61] before interpreting the physicality of the segregation behavior shown in Fig. 3.

B. Segregation Subspectra from QM-MM

In Ref. [61], the authors calculated segregation spectra for Al-based binary systems using a hybrid quantum mechanical/molecular mechanical method and shown that the method used can provide site-wise segregation energy close to a full quantum mechanical treatment. We will therefore analyze these 39 Al(X) systems to provide the most accurate TJ segregation data available to date. Since the computational method for all 39 systems is identical, here we can analyze the full subspectra for both GBs and TJs. All of the resulting spectra for both GB and TJ are presented in Supplementary Table SII [76]. As a brief summary of those data, we also visualize the index J_X using the periodic table plot of Fig. 4 with the identical color scale as Fig. 3.

We observe greater tendency for junction segregation in general for these quantum-accurate systems, as visualized in the color scale of Fig. 4 (the magnitude of the negative indices, when they occur, is always less than 0.1). The most extreme junction segregation indices are also found near the partially-filled d-block elements such as Ti, Nb and Ta. Interestingly, this trend seems to have stronger chemical effects unlike the segregation strength itself (which is shown in Fig. 3 of Ref. [61]). For example, even though Al(Zr) and Al(Cu) have similar segregation strengths, we observe much stronger junction segregation for Al(Zr). Such data point to interesting experimental directions for the study of TJ segregation.

C. Physicality of Interatomic Potentials

The question of interatomic potentials' relevance to the segregation problem is certainly important for interpreting the data in Fig. 3. With quantum-accurate data available (Fig. 4), we are in a position to evaluate potentials directly on the basis of their accuracy for segregation behavior. In Fig. 5 we show Al(Ni) spectra from two binary interatomic potentials [53,54] in Fig. 5a. This comparison puts a point on the role of the potentials, as these two systems for nominally the same alloy system exhibit the opposite GB and TJ preferences, and have extremely different overall spectra. Unfortunately, neither of the potentials is close to the QM-MM result [61] which is also plotted in Fig. 5a, and show behavior that lies between that of the two potentials from Fig. 5a (i.e. no strong preference for either GBs or TJs). It should also be noted that the magnitudes of segregation energies are also drastically different amongst these approaches, as suggested by the vertical lines (means) in Fig. 5a.

The discrepancies between the segregation spectra in Fig. 5a are likely artefacts of either the specific methods of calculating the electronic-level data to which the potentials are fitted, or of the fitting itself, or both. Potential development depends significantly on the problems of interest to the developer, and accurate representation of GB and TJ segregation is not a conventional goal of fitting [44,77–80]. We might speculate that interatomic potentials fitted for disordered structures such as grain boundaries, metallic glasses and liquid systems should achieve better accuracy for this specific problem due to the similarity of the structural environments [81–83]. We explore this conjecture briefly in what follows.

Example subspectra are provided from the Al(Zr) EAM potential by Cheng *et al.* [47], which was developed using several atomic configurations including liquid inherent structures, and also validated with structure factors from extended X-ray absorption fine structure measurements. The comparison of the segregation spectra based on this potential and on QM-MM are shown in Fig. 5b; they are quite comparable, with the same junction preference and accuracy of the full spectrum to within about 5 kJ/mol on a spectrum spanning more than 100 kJ/mol. This level of matching is probably reasonable for many quantitative purposes, and very encouraging.

A second comparison case is provided by the Al(Ag) potential from Sheng [43] in Fig. 5c. This potential was developed by including liquid configurations in the fitting data. While the potential produces the same J_X sign as the QM-MM results, it has a significantly different spectral shape and width. Thus, while some potentials may reproduce the same relative shift between GB and TJ sites, i.e., the same sign and even magnitude of J_X, this does not speak to the spectral shape itself unless the disordered structures used for fitting present a good match to the atomic environments of the intergranular network.

Unfortunately, we tentatively conclude that in general, EAM potentials should be used with care for the prediction of intergranular segregation, even when fitted to some irregular environments. However, we note that QM-MM calculations are hybrid calculations [61,84–86], and while they have been validated for GB sites, they are not yet specifically validated against full quantum calculations for the more complex TJ sites. Full electronic computation of such large polycrystalline systems is still intractable with current computational facilities, so such a validation must await computational advances. However, the fact that all methods explored here seem to predict a similar shift of segregation energies from GBs to TJs supports some degree of trust in the QM/MM results for TJs.

One interesting point of agreement among the EAM and QM-MM approaches is that there are some alloy systems with negative J_X (Fig. 4), i.e., those in which segregant favors GBs over TJs. While this is somewhat counterintuitive, it may indeed be physical based on the present set of computations. Fig. 4 suggests that for the more accurate QM-MM results this behavior is very weak at best: the magnitude of the positive J_X values from the QM-MM here is always low (less than 0.1), whereas the TJ segregating favoring systems have J_X values that are of much higher magnitude—as high as 0.4 for Al(Nb) and Al(Ta). The Al(Co, Cr, Fe, Ni) systems in Fig. 4 lie near the borderline of zero J_X which indicates that the junction effects in these systems are small; in reality these alloys apparently would not prefer GBs as strongly as the EAM potentials of Ref. [44] in Fig. 3 might suggest. This result again stresses the fact that some of the EAM potentials in the literature are optimized for conditions sufficiently far from the problem of GB/TJ segregation as to quantitatively miss the full physics of the problem [44].

D. Driving Forces for Segregation

There are many advantages of having a large database of quantum-accurate segregation energies associated with specific sites in specific defects. Among these is the ability to examine the local site features that are associated with segregation, since every system shown in Fig. 4 was calculated using the same procedure. For example, in Fig. 6 we show the distribution of local atomic volume and coordination number obtained from Voronoi analysis [87,88] for all of the GB and TJ sites. These data are taken from the pure polycrystals used to calculate the QM-MM spectra. There are several interesting observations in these data.

First, we observe slightly lower atomic volumes among TJ sites (slight shift in Fig. 6a) and higher coordination (taller bars for Z>12 in Fig. 6b) as compared with GB sites. In other words, TJs in aluminum are slightly more closely packed than grain boundaries in an average sense. This would be expected to have implications for solute segregation: such tighter TJ sites could be more energetically preferred for relatively smaller segregants, for example. As an illustration, we compare Ti (J_{Ti} = 0.37) to Hf (J_{Hf} = 0.31) since both elements have the same crystal structure and also a similar bulk modulus [89], and thus the biggest physical difference between these solutes is their size: Hf has an atomic volume of 22.34 while Ti is 17.57 Å^3. The larger size of Hf results in the clustering of negative segregation sites near large atomic volume sites for Hf in Fig. 6d, and these are more likely to lie in the GB regions (cf. Fig. 6a,b). Conversely, the smaller Ti preferentially selects small, tightly packed sites as in Fig. 6c, and these tend to be more in the TJs. This elastic effect reflects in the overall higher junction segregation index of Al(Ti). Lastly, while some average segregation trend can be qualitatively explained via the Miedema elastic relaxation model [61], the atomic environment difference between GBs and TJs may allow different degrees of elastic relaxation and chemical bonding (not fully relaxed as assumed in Miedema model [90]), resulting in a more complicated segregation response. We leave a more thorough analysis of the local GB and TJ atomic environments and their correlation to segregation strength for our future work.

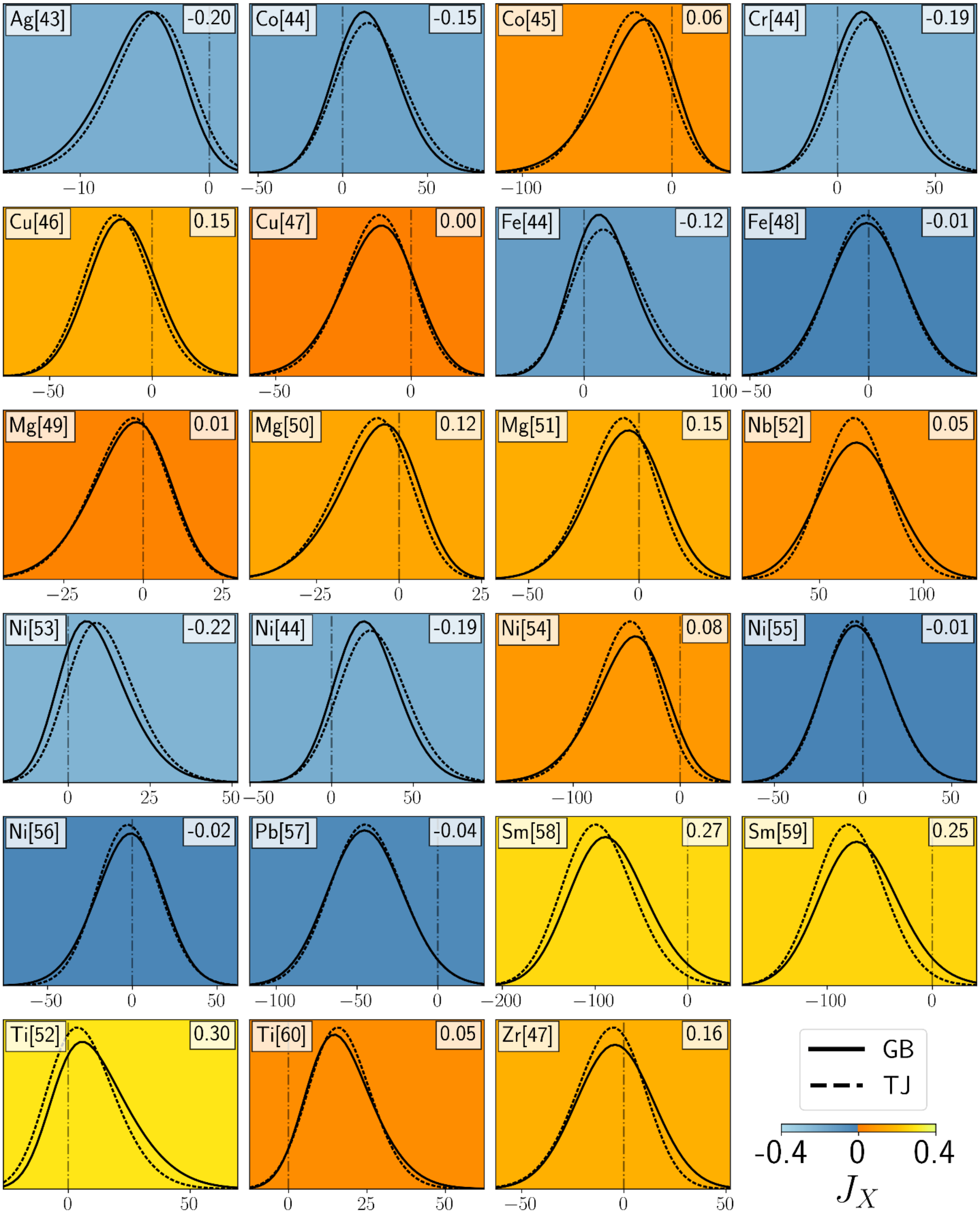

FIG. 3. Segregation subspectra predicted by 23 EAM potentials [43–60] in kJ/mol with the junction indices labeled at the top-right corner of the plots.

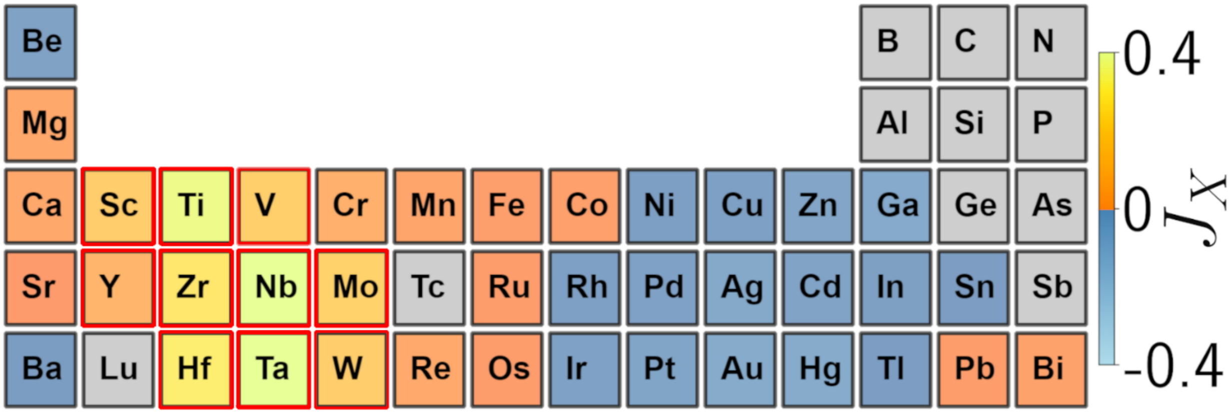

FIG. 4. Periodic table plot of the junction segregation index J_x as defined in Eq. (5), based on quantum-accurate segregation spectra rather than potentials. The systems with an index of higher than 0.1 in the magnitude are bordered in red.

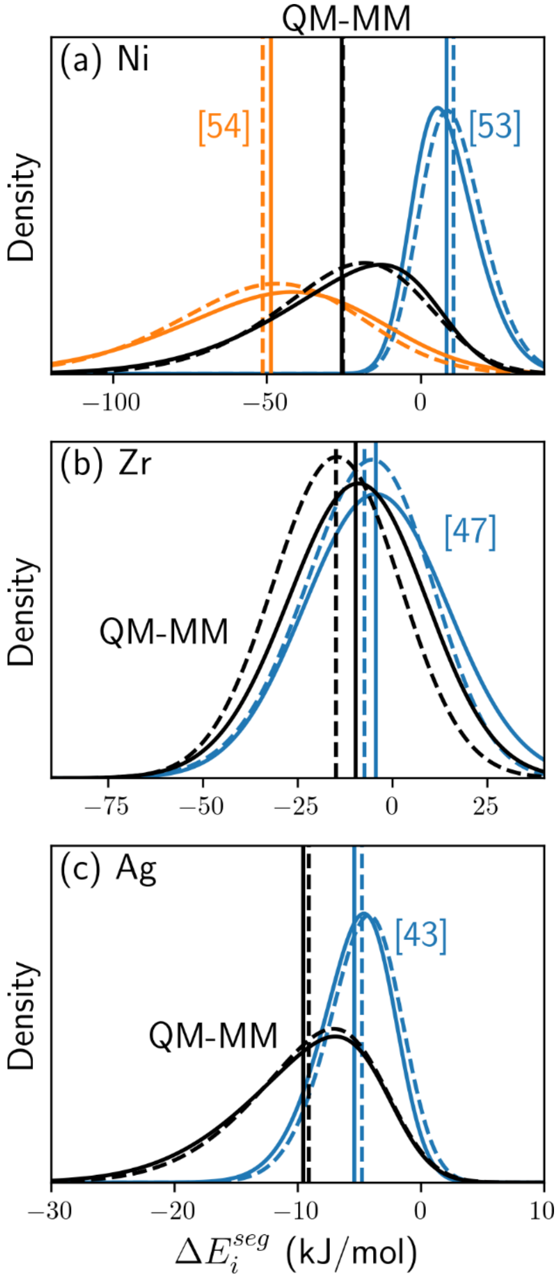

FIG. 5. A comparison of EAM potentials (in color) with quantum-accurate QM-MM segregation spectra (in black). GB and TJ subspectra are labeled with solid and dashed lines respectively. (a) Defect subspectra of Al(Ni) EAM systems (Ref. [53] and [54]), (b) Al(Zr) [47] and (c) Al(Ag) [43]. The QM-MM data from Ref. [61] for each corresponding system are also plotted in (a-c). The vertical lines indicating the mean are also plotted to demonstrate the GB/TJ relative shifts.

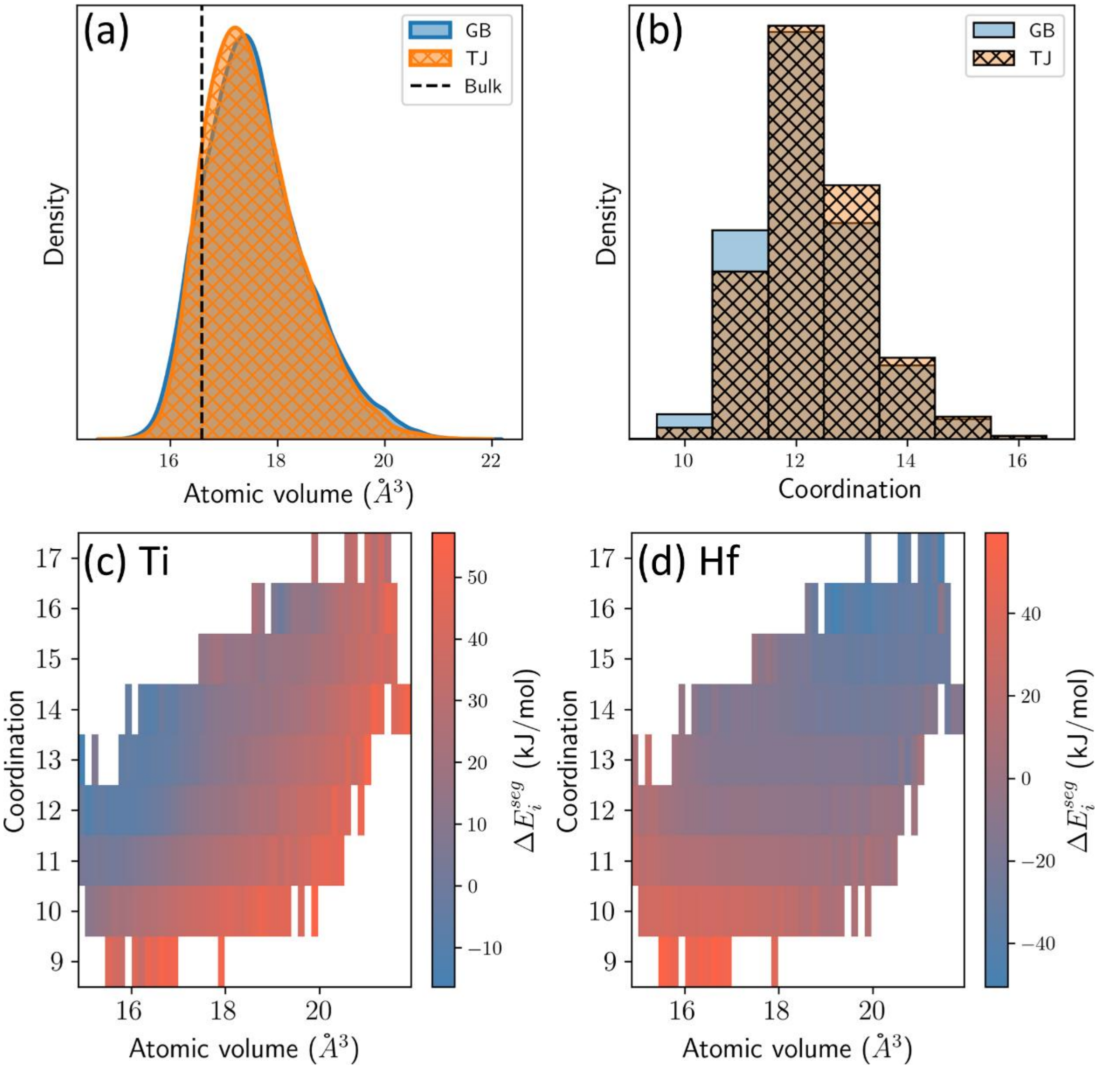

FIG. 6. (a) Atomic volume and (b) coordination number distribution of GB and TJ sites. The scatter plot of both (a) and (b) are combined in (c) for Al(Ti) and (d) for Al(Hf). The colormap in (c) and (d) denotes the average site-wise segregation energy of the sites within the box range.

IV. Grain Size Dependencies

The importance of TJ segregation is especially acute at the finest nanocrystalline grain sizes, where the volume fraction of TJ sites increases rapidly with decreasing grain size. This has an impact on the overall segregation behavior through the solute balance amongst the various site types [91]:

$$X^{tot} = (1 - f^{GB} - f^{TJ})X^{C} + f^{GB}\bar{X}^{GB} + f^{TJ}\bar{X}^{TJ} \tag{6}$$

where s is the defect order which can be grain boundary (*s* = GB) or triple junctions (*s* = TJ), and $\bar{X}^{s}$ is the average solute concentration for the defect order *s*. The volume fractions f^{s} scale with the grain size following power-laws based on polycrystalline geometry *[11,92–95]*. These may be expressed in a general form *[42]*, modified here to roll quadruple nodes into the TJ population:

$$f^s = A_3^s\left(\frac{\alpha}{d}\right)^3 + A_2^s\left(\frac{\alpha}{d}\right)^2 + A_1^s\left(\frac{\alpha}{d}\right) \tag{7}$$

$$d = 2\frac{L}{(N\frac{4}{3}\pi)^{1/3}} \tag{8}$$

where α is the intergranular dimension and d is the grain size defined as the spherical equivalent grain size by assuming that the volume of a cube of length L equally contributes to N spherical grains of diameter d. The defect fractions of Eqs. (7) are plotted in Fig. 7 for d = 2-100 nm with the parameters listed in Table I, and alternate but essentially equivalent forms are included in the supplemented software (see Supplementary Material SM. 4 [76]). Similar to Eq. (1), the "effective" segregation energy of a defect type s ($\Delta\bar{E}_{Eff}^s$) can be calculated by solving the equation:

$$\frac{\bar{X}^s}{1-\bar{X}^s} = \frac{X^C}{1-X^C} exp\left[-\frac{\Delta\bar{E}_{eff}^s}{k_bT}\right] \tag{9}$$

The thermodynamic model of Eqs. (2-4,6-9) is solved numerically [20,28,42] to attain a rigorous view of segregation amongst all site types in the polycrystalline environment.

This spectral model can give rich information about temperature, composition, and grain size dependencies on segregation phenomena in all of the alloys across Fig. 4, and the data needed to perform such analyses are fully incorporated in the Supplementary Materials SM. 4 [76]. For the sake of a simple illustration, here we limit the discussion to a single case of Al(Nb). This system is selected because it has one of the highest TJ selectivities (Fig. 4), and thus presents something of an extreme case for the excess segregation that can be expected in very fine nanocrystalline aluminum from the presence of TJs. To understand grain size dependencies, the results can be back-fitted to the McLean isotherm of Eq. (1), which assumes no spectral behavior and no associated size dependencies. In Ref. [42] we discussed all the possible grain size dependencies in this kind of analysis, and here we are concerned with just one: the role of TJs in producing excess segregation. Therefore, here we calculate the intergranular excess, β ($\bar{X}^{IG}/X^C$), and effective segregation energy and extract the TJ effects by comparing the full output of the isotherm (inclusive of TJs) with the solutions calculated in the same way but without including the TJ subspectrum.

The junction effects of β and $\Delta\bar{E}_{eff}^s$ are plotted in Fig. 8a and 8b respectively, for both "with TJs" and "without TJs" cases. The normalized β and $\Delta\bar{E}_{eff}^s$ are also plotted in Fig. 8c and 8d respectively to explicitly show their fractional rises due to the presence of TJs (i.e. with the spectral effects excluded). We will first focus on a constant 1% solute addition, X^{tot} = 0.01 (solid lines) in Fig. 8. We observe a drastic increase in β of more than 1 at grain sizes less than 12 nm in Fig. 8a, which can result in as much as 3 kJ/mol difference in the McLean effective segregation energy as shown in Fig. 8b. These increments are about the same magnitude as the isotherm solutions as shown in Fig. 8c and 8d (TJs contribute more than 30% to the solute enrichment β in Fig. 8c at grain sizes roughly less than 12 nm, and can double at the finest grain sizes). As physically expected, we observe negligible TJ effects at grain sizes of larger than roughly 40 nm where both the excess solute and apparent segregation energies in Fig. 8 converge; triple junctions become volumetrically negligible at this size range (cf. Fig. 7).

Such grain size dependence can also be a function of temperature and concentration in a closed system, which shift the solute occupancies amongst various sites in the intergranular network [28,42,96]. To demonstrate this issue, we show a similar size dependence analysis for $X^{tot} = 0.05$ for comparison (dash-dot lines). The lower total solute concentrations at $X^{tot} = 0.01$ lead to more the solute atoms occupying the negative tail of the distribution. This consequently leads to stronger junction effects in Fig. 8 (larger β and $\Delta\bar{E}_{eff}^{seg}$ differences). The dependencies observed are also caused by the subspectral distribution parameters which are system dependent (cf. parameters in Supplementary Table SI and SII [76]). Even though these issues are not easily simplified, the example code supplemented here can be adjusted to the material (α, μ and σ) and experimental (d, X^{tot} and T) parameters of interest. The information of the attached software written with Python packages [97–104] can be found in the Supplementary Material [76], including how Fig. 8 was calculated.

TABLE I. Fitted geometrical parameters for use with Eqs. (8)

s	α (nm)	A_3	A_2	A_1
GB	1.09	2.65	-4.33	1.68
TJ		-2.70	3.70	0.0

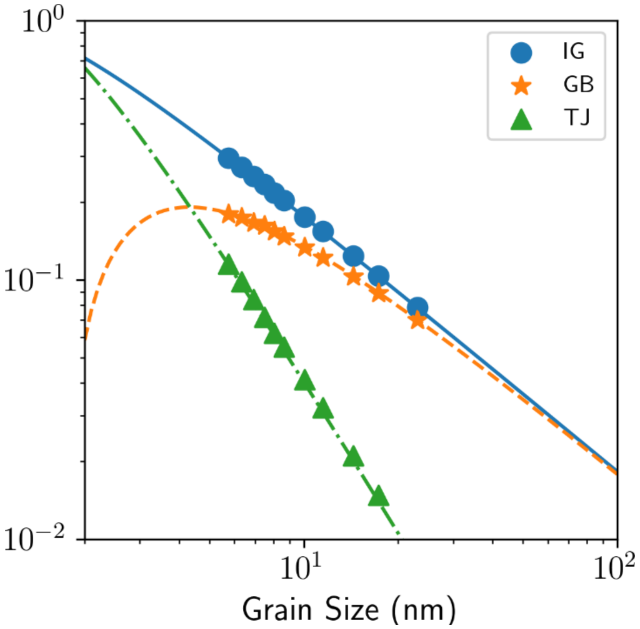

FIG. 7. Intergranular, grain boundary and triple junction defect fraction fitted from the self-similarly scaled polycrystals.

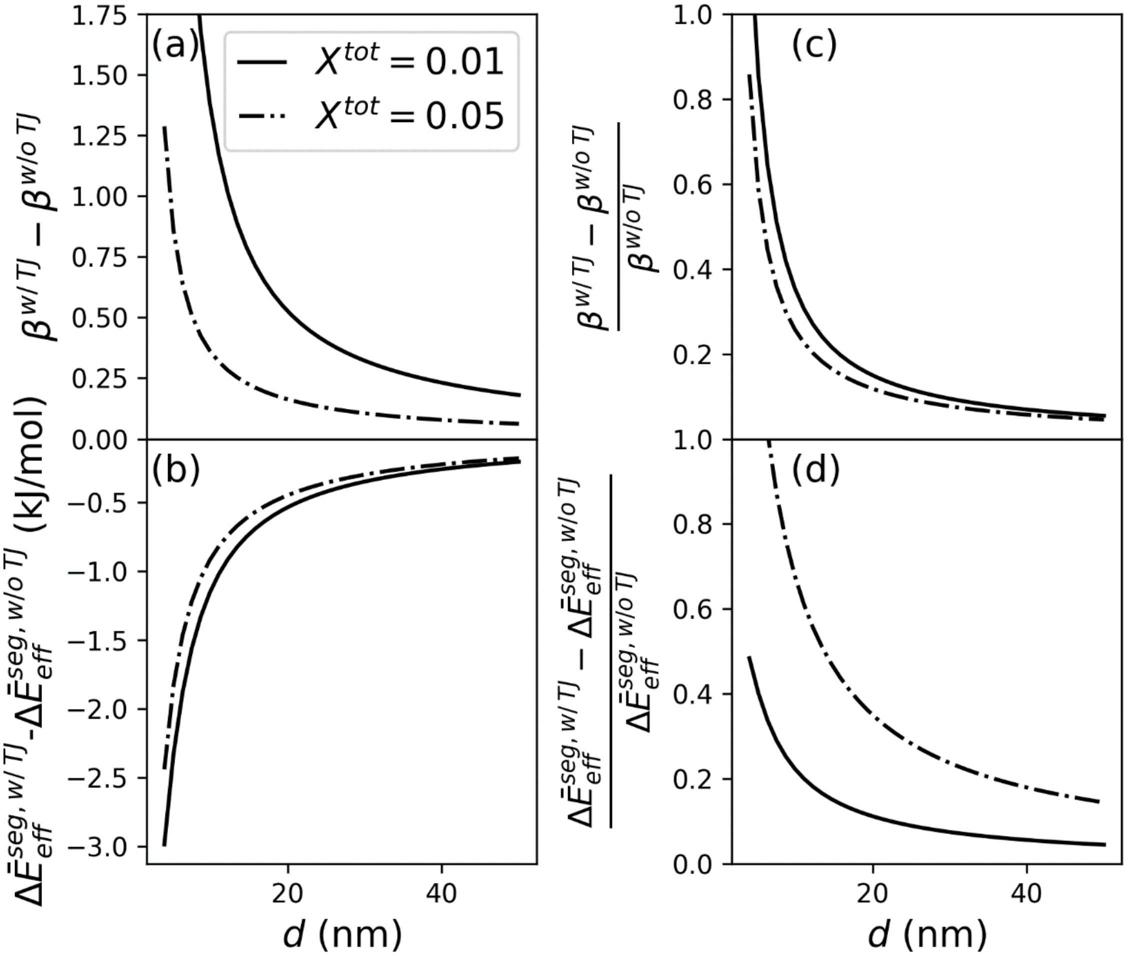

FIG. 8. Physical junction effects or the differences between the solutions with "scaled" (TJs included) and "non-scaled" (only GBs) spectra are plotted in (a) for the solute enrichment (β) and (b) for the effective segregation energy ($\Delta\bar{E}_{eff}^{seg}$). (a) and (b) are normalized with the "w/o TJs" solutions to demonstrate the relative increments if TJs are included.

V. Conclusion

Triple junction segregation behavior is demonstrated via molecular statics and a defect-identifying algorithm for 23 dilute EAM Al-based binary systems with available interatomic potentials, and 39 QM-MM spectra generated via machine learning data. In addition to the development of a large library of triple junction segregation spectra that should be useful for alloy screening and the guidance of experimental work, this study led to several physically salient points:

- Most alloys seem to favor triple junction segregation over grain boundary segregation, and this becomes more true as the accuracy of the analysis increases from EAM to QM-MM. Very few systems at QM-MM accuracy seem to have a physical preference for GB segregation, and this preference is rather slight in those systems. By contrast, the preference of some solutes for TJ sites vis-à-vis GB ones can be quite strong.

- The comparison between EAM and QM-MM systems in Fig. (5) stresses that EAM potentials may not be relevant for intergranular segregation applications, which may generally involve structures far from the potential fitting data.
- The strong triple junction segregating QM-MM systems cluster near partially-filled d-block transition metals such as Sc, Ti, Zr, Nb and Ta, suggesting a periodic trend for this phenomenon.
- The exclusion of triple junctions does not result in significant errors of the bulk behavior for large grain sizes of more than approximately 40 nm but can still cause significantly elevated local solute concentrations at grain junctions. The magnitude of junction effects depends on the system.
- The information and software provided in the supplemental data can be applied to a specific experimental/computational situation of interest for all of the Al alloys studied here.

The framework established here is not limited to FCC materials and as more electronic calculations of the segregation spectra become available should be useful to understand triple junction segregation in, e.g., steel, nickel and magnesium alloys. Given the sparsity and heterogeneity of triple junction experimental data [38,41,105,106] available to date, it is hoped that the present approach of identifying alloys with strong GB/TJ contrast (Fig. 3 and 4) could point to interesting directions for focused experimentation, or incorporating the framework in intergranular segregation kinetic models [107–112] to explain intergranular solute heterogeneity observed in nanocrystals.

VI. Acknowledgments

This work was supported by the US Department of Energy award No. DE-SC0020180. The authors acknowledge MIT Satori and Research Computing Project for computational resources used in this work. N. Tuchinda acknowledges the financial support from Anandamahidol Foundation Scholarship and fruitful discussions with M. Wagih and T. Matson. We also would like to thank M. Wagih for providing us the first-principles polycrystalline solute segregation database from Ref. [61].

VII. References

[1] H. Gleiter, *Nanostructured Materials: Basic Concepts and Microstructure*, Acta Materialia **48**, 1 (2000).

[2] H. Gleiter, *Nanostructured Materials: State of the Art and Perspectives*, Nanostructured Materials **6**, 3 (1995).

[3] K. S. Kumar, H. Van Swygenhoven, and S. Suresh, *Mechanical Behavior of Nanocrystalline Metals and Alloys11The Golden Jubilee Issue—Selected Topics in Materials Science and Engineering: Past, Present and Future, Edited by S. Suresh*, Acta Materialia **51**, 5743 (2003).

[4] M. A. Meyers, A. Mishra, and D. J. Benson, *Mechanical Properties of Nanocrystalline Materials*, Progress in Materials Science **51**, 427 (2006).

[5] D. G. Morris and M. A. Morris, *Microstructure and Strength of Nanocrystalline Copper Alloy Prepared by Mechanical Alloying*, Acta Metallurgica et Materialia **39**, 1763 (1991).

[6] Y. Wan, B. Tang, Y. Gao, L. Tang, G. Sha, B. Zhang, N. Liang, C. Liu, S. Jiang, Z. Chen, et al., *Bulk Nanocrystalline High-Strength Magnesium Alloys Prepared via Rotary Swaging*, Acta Materialia **200**, 274 (2020).

[7] K. M. Youssef, R. O. Scattergood, K. L. Murty, and C. C. Koch, *Nanocrystalline Al–Mg Alloy with Ultrahigh Strength and Good Ductility*, Scripta Materialia **54**, 251 (2006).

[8] V. Y. Gertsman and R. Birringer, *On the Room-Temperature Grain Growth in Nanocrystalline Copper*, Scripta Metallurgica et Materialia **30**, 577 (1994).

[9] J. Weissmüller, *Alloy Effects in Nanostructures*, Nanostructured Materials **3**, 261 (1993).

[10] J. Weissmüller, *Some Basic Notions on Nanostructured Solids*, Materials Science and Engineering: A **179–180**, 102 (1994).

[11] J. R. Trelewicz and C. A. Schuh, *Grain Boundary Segregation and Thermodynamically Stable Binary Nanocrystalline Alloys*, Phys. Rev. B **79**, 094112 (2009).

[12] A. R. Kalidindi and C. A. Schuh, *Stability Criteria for Nanocrystalline Alloys*, Acta Materialia **132**, 128 (2017).

[13] T. Chookajorn, H. A. Murdoch, and C. A. Schuh, *Design of Stable Nanocrystalline Alloys*, Science **337**, 951 (2012).

[14] M. Hillert, *Solute Drag, Solute Trapping and Diffusional Dissipation of Gibbs Energy11This Paper Is Based on the Hume–Rothery Lecture Presented at the 128th TMS Annual Meeting, 1 March 1999, San Diego, U.S.A.*, Acta Materialia **47**, 4481 (1999).

[15] M. Hillert, *Solute Drag in Grain Boundary Migration and Phase Transformations*, Acta Materialia **52**, 5289 (2004).

[16] S. G. Kim and Y. B. Park, *Grain Boundary Segregation, Solute Drag and Abnormal Grain Growth*, Acta Materialia **56**, 3739 (2008).

[17] M. Alkayyali and F. Abdeljawad, *Grain Boundary Solute Drag Model in Regular Solution Alloys*, Phys. Rev. Lett. **127**, 175503 (2021).

[18] A. Suhane, D. Scheiber, M. Popov, V. I. Razumovskiy, L. Romaner, and M. Militzer, *Solute Drag Assessment of Grain Boundary Migration in Au*, Acta Materialia **224**, 117473 (2022).

[19] D. McLean and A. Maradudin, *Grain Boundaries in Metals* (Clarendon Press, Oxford, 1957).

[20] C. White and D. Stein, *Sulfur Segregation to Grain Boundaries in Ni 3 Al and Ni 3 (Al, Ti) Alloys*, Metallurgical Transactions A **9**, 13 (1978).

[21] M. N. Kelly, K. Glowinski, N. T. Nuhfer, and G. S. Rohrer, *The Five Parameter Grain Boundary Character Distribution of α-Ti Determined from Three-Dimensional Orientation Data*, Acta Materialia **111**, 22 (2016).

[22] S. Ratanaphan, Y. Yoon, and G. S. Rohrer, *The Five Parameter Grain Boundary Character Distribution of Polycrystalline Silicon*, J Mater Sci **49**, 4938 (2014).

[23] V. Randle, G. S. Rohrer, H. M. Miller, M. Coleman, and G. T. Owen, *Five-Parameter Grain Boundary Distribution of Commercially Grain Boundary Engineered Nickel and Copper*, Acta Materialia **56**, 2363 (2008).

[24] S. Patala, *Understanding Grain Boundaries – The Role of Crystallography, Structural Descriptors and Machine Learning*, Computational Materials Science **162**, 281 (2019).

[25] E. R. Homer, D. M. Hensley, C. W. Rosenbrock, A. H. Nguyen, and G. L. W. Hart, *Machine-Learning Informed Representations for Grain Boundary Structures*, Front. Mater. **6**, 168 (2019).

[26] L. Huber, R. Hadian, B. Grabowski, and J. Neugebauer, *A Machine Learning Approach to Model Solute Grain Boundary Segregation*, Npj Comput Mater **4**, 64 (2018).

[27] Y. Mahmood, M. Alghalayini, E. Martinez, C. J. J. Paredis, and F. Abdeljawad, *Atomistic and Machine Learning Studies of Solute Segregation in Metastable Grain Boundaries*, Sci Rep **12**, 6673 (2022).

[28] M. Wagih and C. A. Schuh, *Spectrum of Grain Boundary Segregation Energies in a Polycrystal*, Acta Materialia **181**, 228 (2019).

[29] A. Azzalini and A. Capitanio, *Statistical Applications of the Multivariate Skew Normal Distribution*, Journal of the Royal Statistical Society: Series B (Statistical Methodology) **61**, 579 (1999).

[30] M. Wagih, P. M. Larsen, and C. A. Schuh, *Learning Grain Boundary Segregation Energy Spectra in Polycrystals*, Nat Commun **11**, 6376 (2020).

[31] G. Palumbo, S. J. Thorpe, and K. T. Aust, *On the Contribution of Triple Junctions to the Structure and Properties of Nanocrystalline Materials*, Scripta Metallurgica et Materialia **24**, 1347 (1990).

[32] B. Zhao, G. Gottstein, and L. S. Shvindlerman, *Triple Junction Effects in Solids*, Acta Materialia **59**, 3510 (2011).

[33] A. H. Chokshi, *Triple Junction Limited Grain Growth in Nanomaterials*, Scripta Materialia **59**, 726 (2008).

[34] G. Gottstein, A. H. King, and L. S. Shvindlerman, *The Effect of Triple-Junction Drag on Grain Growth*, Acta Materialia **48**, 397 (2000).

[35] Y. Zhou, U. Erb, K. Aust, and G. Palumbo, *The Effects of Triple Junctions and Grain Boundaries on Hardness and Young's Modulus in Nanostructured Ni–P*, Scripta Materialia **48**, 825 (2003).

[36] U. Czubayko, V. G. Sursaeva, G. Gottstein, and L. S. Shvindlerman, *Influence of Triple Junctions on Grain Boundary Motion*, Acta Materialia **46**, 5863 (1998).

[37] I. Ovid'ko, *Triple Junction Nanocracks in Deformed Nanocrystalline Materials*, Acta Materialia **52**, 1201 (2004).

[38] K.-M. Yin, A. H. King, T. E. Hsieh, F.-R. Chen, J. J. Kai, and L. Chang, *Segregation of Bismuth to Triple Junctions in Copper*, Microsc Microanal **3**, 417 (1997).

[39] S. M. Eich and G. Schmitz, *Embedded-Atom Study of Low-Energy Equilibrium Triple Junction Structures and Energies*, Acta Materialia **109**, 364 (2016).

[40] G. Gottstein, Y. Ma, and L. Shvindlerman, *Triple Junction Motion and Grain Microstructure Evolution*, Acta Materialia **53**, 1535 (2005).

[41] J. Tian and Y.-L. Chiu, *Study the Grain Boundary Triple Junction Segregation of Phosphorus in a Nickel-Base Alloy Using Energy Dispersive X-Ray Spectroscopy on a Transmission Electron Microscope*, Materials Characterization **148**, 156 (2019).

[42] N. Tuchinda and C. A. Schuh, *Grain Size Dependencies of Intergranular Solute Segregation in Nanocrystalline Materials*, Acta Materialia **226**, 117614 (2022).

[43] H. Sheng, *Al-Ag EAM Potential, Private Communication*, https://sites.google.com/site/eampotentials/AlAg (n.d.).

[44] D. Farkas and A. Caro, *Model Interatomic Potentials for Fe–Ni–Cr–Co–Al High-Entropy Alloys*, J. Mater. Res. **35**, 3031 (2020).

[45] G. P. Pun, V. Yamakov, and Y. Mishin, *Interatomic Potential for the Ternary Ni–Al–Co System and Application to Atomistic Modeling of the B2–L10 Martensitic Transformation*, Modelling and Simulation in Materials Science and Engineering **23**, 065006 (2015).

[46] X.-Y. Liu, C.-L. Liu, and L. Borucki, *A New Investigation of Copper's Role in Enhancing Al–Cu Interconnect Electromigration Resistance from an Atomistic View*, Acta Materialia **47**, 3227 (1999).

[47] Y. Q. Cheng, E. Ma, and H. W. Sheng, *Atomic Level Structure in Multicomponent Bulk Metallic Glass*, Phys. Rev. Lett. **102**, 245501 (2009).

[48] M. I. Mendelev, D. J. Srolovitz, G. J. Ackland, and S. Han, *Effect of Fe Segregation on the Migration of a Non-Symmetric ∑5 Tilt Grain Boundary in Al*, Journal of Materials Research **20**, 208 (2005).

[49] X.-Y. Liu, P. P. Ohotnicky, J. B. Adams, C. L. Rohrer, and R. W. Hyland, *Anisotropic Surface Segregation in Al⍰Mg Alloys*, Surface Science **373**, 357 (1997).

[50] X.-Y. Liu and J. B. Adams, *Grain-Boundary Segregation in Al–10%Mg Alloys at Hot Working Temperatures*, Acta Materialia **46**, 3467 (1998).

[51] M. I. Mendelev, M. Asta, M. J. Rahman, and J. J. Hoyt, *Development of Interatomic Potentials Appropriate for Simulation of Solid–Liquid Interface Properties in Al–Mg Alloys*, Philosophical Magazine **89**, 3269 (2009).

[52] D. Farkas and C. Jones, *Interatomic Potentials for Ternary Nb-Ti-Al Alloys*, Modelling and Simulation in Materials Science and Engineering **4**, 23 (1996).

[53] J. E. Angelo, N. R. Moody, and M. I. Baskes, *Trapping of Hydrogen to Lattice Defects in Nickel*, Modelling and Simulation in Materials Science and Engineering **3**, 289 (1995).

[54] Y. Mishin, M. Mehl, and D. Papaconstantopoulos, *Embedded-Atom Potential for B 2− NiAl*, Physical Review B **65**, 224114 (2002).

[55] Y. Mishin, *Atomistic Modeling of the γ and Γ′-Phases of the Ni–Al System*, Acta Materialia **52**, 1451 (2004).

[56] G. Purja Pun and Y. Mishin, *Development of an Interatomic Potential for the Ni-Al System*, Philosophical Magazine **89**, 3245 (2009).

[57] A. Landa, P. Wynblatt, D. Siegel, J. Adams, O. Mryasov, and X.-Y. Liu, *Development of Glue-Type Potentials for the Al–Pb System: Phase Diagram Calculation*, Acta Materialia **48**, 1753 (2000).

[58] H. Song and M. I. Mendelev, *Molecular Dynamics Study of Mechanism of Solid–Liquid Interface Migration and Defect Formation in Al3Sm Alloy*, JOM **73**, 2312 (2021).

[59] M. Mendelev, F. Zhang, Z. Ye, Y. Sun, M. Nguyen, S. Wilson, C. Wang, and K. Ho, *Development of Interatomic Potentials Appropriate for Simulation of Devitrification of Al90Sm10 Alloy*, Modelling and Simulation in Materials Science and Engineering **23**, 045013 (2015).

[60] R. R. Zope and Y. Mishin, *Interatomic Potentials for Atomistic Simulations of the Ti-Al System*, Physical Review B **68**, 024102 (2003).

[61] M. Wagih and C. A. Schuh, *Learning Grain-Boundary Segregation: From First Principles to Polycrystals*, Phys. Rev. Lett. **129**, 046102 (2022).

[62] P. Hirel, *Atomsk: A Tool for Manipulating and Converting Atomic Data Files*, Computer Physics Communications **197**, 212 (2015).

[63] M. S. Daw, S. M. Foiles, and M. I. Baskes, *The Embedded-Atom Method: A Review of Theory and Applications*, Materials Science Reports **9**, 251 (1993).

[64] M. S. Daw and M. I. Baskes, *Embedded-Atom Method: Derivation and Application to Impurities, Surfaces, and Other Defects in Metals*, Phys. Rev. B **29**, 6443 (1984).

[65] V. Jambur, C. Tangpatjaroen, J. Xi, J. Tarnsangpradit, M. Gao, H. Sheng, J. Perepezko, and I. Szlufarska, *Effects of Minor Alloying on the Mechanical Properties of Al Based Metallic Glasses*, Journal of Alloys and Compounds **854**, 157266 (2021).

[66] S. Plimpton, *Fast Parallel Algorithms for Short-Range Molecular Dynamics*, Journal of Computational Physics **117**, 1 (1995).

[67] W. M. Brown, P. Wang, S. J. Plimpton, and A. N. Tharrington, *Implementing Molecular Dynamics on Hybrid High Performance Computers–Short Range Forces*, Computer Physics Communications **182**, 898 (2011).

[68] W. M. Brown, A. Kohlmeyer, S. J. Plimpton, and A. N. Tharrington, *Implementing Molecular Dynamics on Hybrid High Performance Computers–Particle–Particle Particle-Mesh*, Computer Physics Communications **183**, 449 (2012).

[69] W. M. Brown and M. Yamada, *Implementing Molecular Dynamics on Hybrid High Performance Computers—Three-Body Potentials*, Computer Physics Communications **184**, 2785 (2013).

[70] A. Stukowski, *Visualization and Analysis of Atomistic Simulation Data with OVITO–the Open Visualization Tool*, Modelling and Simulation in Materials Science and Engineering **18**, 015012 (2009).

[71] J. F. Panzarino and T. J. Rupert, *Tracking Microstructure of Crystalline Materials: A Post-Processing Algorithm for Atomistic Simulations*, JOM **66**, 417 (2014).

[72] P. M. Larsen, S. Schmidt, and J. Schiøtz, *Robust Structural Identification via Polyhedral Template Matching*, Modelling and Simulation in Materials Science and Engineering **24**, 055007 (2016).

[73] N. Wang, G. Palumbo, Z. Wang, U. Erb, and K. T. Aust, *On the Persistence of Four-Fold Triple Line Nodes in Nanostructured Materials*, Scripta Metallurgica et Materialia **28**, 253 (1993).

[74] J. D. Honeycutt and H. C. Andersen, *Molecular Dynamics Study of Melting and Freezing of Small Lennard-Jones Clusters*, Journal of Physical Chemistry **91**, 4950 (1987).

[75] A. Stukowski, *Structure Identification Methods for Atomistic Simulations of Crystalline Materials*, Modelling Simul. Mater. Sci. Eng. **20**, 045021 (2012).

[76] See Supplemental Material at [URL will be inserted by publisher] for the details of validations, calculations and the supplementary software. (n.d.).

[77] M. S. Daw and R. D. Hatcher, *Application of the Embedded Atom Method to Phonons in Transition Metals*, Solid State Communications **56**, 697 (1985).

[78] S. M. Rassoulinejad-Mousavi and Y. Zhang, *Interatomic Potentials Transferability for Molecular Simulations: A Comparative Study for Platinum, Gold and Silver*, Sci Rep **8**, 2424 (2018).

[79] H. W. Sheng, M. J. Kramer, A. Cadien, T. Fujita, and M. W. Chen, *Highly Optimized Embedded-Atom-Method Potentials for Fourteen Fcc Metals*, Phys. Rev. B **83**, 134118 (2011).

[80] X.-Y. Liu, J. B. Adams, F. Ercolessi, and J. A. Moriarty, *EAM Potential for Magnesium from Quantum Mechanical Forces*, Modelling Simul. Mater. Sci. Eng. **4**, 293 (1996).

[81] P. Keblinski, S. R. Phillpot, D. Wolf, and H. Gleiter, *Amorphous Structure of Grain Boundaries and Grain Junctions in Nanocrystalline Silicon by Molecular-Dynamics Simulation*, Acta Materialia **45**, 987 (1997).

[82] T. Brink and K. Albe, *From Metallic Glasses to Nanocrystals: Molecular Dynamics Simulations on the Crossover from Glass-like to Grain-Boundary-Mediated Deformation Behaviour*, Acta Materialia **156**, 205 (2018).

[83] X. Song and C. Deng, *Atomic Energy in Grain Boundaries Studied by Machine Learning*, Phys. Rev. Materials **6**, 043601 (2022).

[84] N. Choly, G. Lu, W. E, and E. Kaxiras, *Multiscale Simulations in Simple Metals: A Density-Functional-Based Methodology*, Phys. Rev. B **71**, 094101 (2005).

[85] Y. Liu, G. Lu, Z. Chen, and N. Kioussis, *An Improved QM/MM Approach for Metals*, Modelling and Simulation in Materials Science and Engineering **15**, 275 (2007).

[86] L. Huber, B. Grabowski, M. Militzer, J. Neugebauer, and J. Rottler, *Ab Initio Modelling of Solute Segregation Energies to a General Grain Boundary*, Acta Materialia **132**, 138 (2017).

[87] G. Voronoi, *Nouvelles Applications Des Paramètres Continus à La Théorie Des Formes Quadratiques. Deuxième Mémoire. Recherches Sur Les Parallélloèdres Primitifs.*, Journal Für Die Reine Und Angewandte Mathematik **134**, 198 (1908).

[88] C. Rycroft, Voro++: A Three-Dimensional Voronoi Cell Library in C++, Lawrence Berkeley National Lab.(LBNL), Berkeley, CA (United States), 2009.

[89] H. Bakker, *Enthalpies in Alloys: Miedema's Semi-Empirical Model* (Trans Tech Publications, 1998).

[90] H. A. Murdoch and C. A. Schuh, *Estimation of Grain Boundary Segregation Enthalpy and Its Role in Stable Nanocrystalline Alloy Design*, J. Mater. Res. **28**, 2154 (2013).

[91] K. Ishida, *Effect of Grain Size on Grain Boundary Segregation*, Journal of Alloys and Compounds **235**, 244 (1996).

[92] A. Detor and C. Schuh, *Grain Boundary Segregation, Chemical Ordering and Stability of Nanocrystalline Alloys: Atomistic Computer Simulations in the Ni–W System*, Acta Materialia **55**, 4221 (2007).

[93] S. C. Pun, W. Wang, A. Khalajhedayati, J. D. Schuler, J. R. Trelewicz, and T. J. Rupert, *Nanocrystalline Al-Mg with Extreme Strength Due to Grain Boundary Doping*, Materials Science and Engineering: A **696**, 400 (2017).

[94] M. Kapoor and G. B. Thompson, *Role of Atomic Migration in Nanocrystalline Stability: Grain Size and Thin Film Stress States*, Current Opinion in Solid State and Materials Science **19**, 138 (2015).

[95] K. Ito, H. Sawada, and S. Ogata, *Theoretical Prediction of Grain Boundary Segregation Using Nano-Polycrystalline Grain Boundary Model*, Mater. Trans. **62**, 575 (2021).

[96] D. Scheiber and L. Romaner, *Impact of the Segregation Energy Spectrum on the Enthalpy and Entropy of Segregation*, Acta Materialia **221**, 117393 (2021).

[97] G. vanRossum, *Python Reference Manual*, Department of Computer Science [CS] (1995).

[98] T. Kluyver, B. Ragan-Kelley, F. Pérez, B. Granger, M. Bussonnier, J. Frederic, K. Kelley, J. Hamrick, J. Grout, S. Corlay, et al., *Jupyter Notebooks – a Publishing Format for Reproducible Computational Workflows*, in *Positioning and Power in Academic Publishing: Players, Agents and Agendas*, edited by F. Loizides and B. Schmidt (IOS Press, 2016), pp. 87–90.

[99] C. R. Harris, K. J. Millman, S. J. van der Walt, R. Gommers, P. Virtanen, D. Cournapeau, E. Wieser, J. Taylor, S. Berg, N. J. Smith, et al., *Array Programming with NumPy*, Nature **585**, 357 (2020).

[100] P. Virtanen, R. Gommers, T. E. Oliphant, M. Haberland, T. Reddy, D. Cournapeau, E. Burovski, P. Peterson, W. Weckesser, J. Bright, et al., *SciPy 1.0: Fundamental Algorithms for Scientific Computing in Python*, Nature Methods **17**, 261 (2020).

[101] R. Piessens, E. de Doncker-Kapenga, C. W. Überhuber, and D. K. Kahaner, *Quadpack: A Subroutine Package for Automatic Integration*, Vol. 1 (Springer Science & Business Media, 2012).

[102] R. P. Brent, *Algorithms for Minimization without Derivatives* (Courier Corporation, 2013).

[103] Joblib Development Team, *Joblib: Running Python Functions as Pipeline Jobs*, (2022).

[104] J. D. Hunter, *Matplotlib: A 2D Graphics Environment*, Computing in Science & Engineering **9**, 90 (2007).

[105] P. Stender, Z. Balogh, and G. Schmitz, *Triple Junction Segregation in Nanocrystalline Multilayers*, Phys. Rev. B **83**, 121407 (2011).

[106] C. J. O'Brien, C. M. Barr, P. M. Price, K. Hattar, and S. M. Foiles, *Grain Boundary Phase Transformations in PtAu and Relevance to Thermal Stabilization of Bulk Nanocrystalline Metals*, Journal of Materials Science **53**, 2911 (2018).

[107] X. Tingdong, *Non-Equilibrium Grain-Boundary Segregation Kinetics*, J Mater Sci **22**, 337 (1987).

[108] X. Tingdong and C. Buyuan, *Kinetics of Non-Equilibrium Grain-Boundary Segregation*, Progress in Materials Science **49**, 109 (2004).

[109] J. Wu and S. Song, *A Unified Model of Grain-Boundary Segregation Kinetics*, Journal of Applied Physics **110**, 063531 (2011).

[110] D. Scheiber, L. Romaner, F. D. Fischer, and J. Svoboda, *Kinetics of Grain Boundary Segregation in Multicomponent Systems – The Example of a Mo-C-B-O System*, Scripta Materialia **150**, 110 (2018).

[111] D. Scheiber, T. Jechtl, J. Svoboda, F. D. Fischer, and L. Romaner, *On Solute Depletion Zones along Grain Boundaries during Segregation*, Acta Materialia **182**, 100 (2020).

[112] D. Scheiber, J. Svoboda, F. D. Fischer, H. J. Böhm, and L. Romaner, *Fully Coupled Segregation and Precipitation Kinetics Model with Ab Initio Input for the Fe-Au System*, Acta Materialia **244**, 118577 (2023).